2009

THE CHANDRA COSMOS SURVEY. I. OVERVIEW AND POINT SOURCE CATALOG

M Elvis

F Civano

C Vignali

S Puccetti

F Fiore

See next page for additional authors

Authors

M Elvis, F Civano, C Vignali, S Puccetti, F Fiore, N Cappelluti, TL Aldcroft, A Fruscione, G Zamorani, A Comastri, M Brusa, R Gilli, T Miyaji, F Damiani, AM Koekemoer, A Finoguenov, H Brunner, CM Urry, J Silverman, V Mainieri, G Hasinger, R Griffiths, M Carollo, H Hao, L Guzzo, A Blain, D Calzetti, C Carilli, P Capak, S Ettori, G Fabbiano, C Impey, S Lilly, B Mobasher, M Rich, M Salvato, DB Sanders, E Schinnerer, N Scoville, P Shopbell, JE Taylor, Y Taniguchi, and M Volonteri

The Chandra COSMOS Survey, I:
Overview and Point Source Catalog

Martin Elvis[1], Francesca Civano[1], Cristian Vignali[2,3], Simonetta Puccetti[4,5], Fabrizio Fiore[5], Nico Cappelluti[6], T. L. Aldcroft[1], Antonella Fruscione[1], G. Zamorani[3], Andrea Comastri[3], Marcella Brusa[6,7], Roberto Gilli[3], Takamitsu Miyaji[8,9], Francesco Damiani[10], Anton Koekemoer[11], Alexis Finoguenov[6,7], Hermann Brunner[6], C.M. Urry[12], John Silverman[13], Vincenzo Mainieri[14], Guenther Hasinger[6,15], Richard Griffiths[16], Marcella Carollo[13], Heng Hao[1], Luigi Guzzo[17], Andrew Blain[18], Daniela Calzetti[19], C. Carilli[20], Peter Capak[21], Stefano Ettori[3], Giuseppina Fabbiano[1], Chris Impey[22], Simon Lilly[13], Bahram Mobasher[23], Michael Rich[24], Mara Salvato[18], D.B. Sanders[25], Eva Schinnerer[26], N. Scoville [18], Patrick Shopbell[18], James E. Taylor[27], Yoshiaki Taniguchi[28], Marta Volonteri[29]

[1]Harvard-Smithsonian Center for Astrophysics, 60 Garden St., Cambridge, MA 02138 USA

[3]INAF−Osservatorio Astronomico di Bologna, Via Ranzani 1, I–40127 Bologna, Italy

[2]Dipartimento di Astronomia, Università degli Studi di Bologna, Via Ranzani 1, I–40127 Bologna, Italy

[4]ASI Science Data Center, via Galileo Galilei, 00044 Frascati Italy

[5]INAF−Osservatorio astronomico di Roma, Via Frascati 33, 00040 Monteporzio Catone, Italy

[6]Max-Planck-Institute für Extraterrestrische Physik, Postfach 1312, 85741, Garching bei München, Germany

[7]University of Maryland, Baltimore County, 1000 Hilltop Circle, Baltimore, MD 21250, USA

[8]Instituto de Astronomía, Universidad Nacional Autónoma de México, Ensenada, México (mailing address: PO Box 439027, San Ysidro, CA, 92143-9027, USA)

[9]Center for Astrophysics and Space Sciences, University of California San Diego, Code 0424, 9500 Gilman Drive, La Jolla, CA 92093, USA

[10]INAF - Osservatorio Astronomico di Palermo, Piazza del Parlamento 1, I-90134 Palermo, Italy

[11]Space Telescope Science Institute, 3700 San Martin Drive, Baltimore, MD 21218 USA

[12]Department of Physics and Yale Center for Astronomy & Astrophysics, Yale University, P.O. Box 208121, New Haven, CT 06520-8121, USA

[13]Department of Physics, Eidgenssische Technische Hochschule-Zurich, CH-8093 Zurich, Switzerland

[14]ESO, Karl-Schwarschild-Strasse 2, D–85748 Garching, Germany

[15]Max-Planck-Institute für Plasmaphysik, Boltzmannstrasse 2, D-85748 Garching bei München

[16]Department of Physics, Carnegie Mellon University, 5000 Forbes Avenue, Pittsburgh, PA 15213 USA

[17]INAF−Osservatorio Astronomico di Brera, via Bianchi 46, 23807 Merate, Italy

[18]California Institute of Technology, MC 105-24, 1200 East California Boulevard, Pasadena, CA 91125 UA

[19]Department of Astronomy, University of Massachusetts, Amherst, MA 01003 USA

[20]National Radio Astronomy Observatory, PO Box O, Socorro NM 87801 USA

[21]Spitzer Science Center, 314-6 Caltech, Pasadena, CA 91125 USA

[22]Steward Observatory, University of Arizona, 933 North Cherry Avenue, Tucson, AZ 85721 USA

[23]Department of Physics and Astronomy, University of California, Riverside, CA 92521 USA

[24]Department of Physics and Astronomy, University of California, Los Angeles, CA 90095 USA

[25]Institute for Astronomy, University of Hawaii, 2680 Woodlawn Dr., Honolulu, HI 96822 USA

[26]Max-Planck-Institut für Astronomie, Königstuhl 17, Heidelberg D-69117, Germany

[27]Department of Physics and Astronomy, University of Waterloo, Waterloo, Ontario, N2L 3G1, Canada

ABSTRACT

The *Chandra* COSMOS Survey (C-COSMOS) is a large, 1.8 Ms, *Chandra* program that has imaged the central 0.5 sq.deg of the COSMOS field (centered at 10^h, $+02^o$) with an effective exposure of $\sim$160 ksec, and an outer 0.4 sq.deg. area with an effective exposure of $\sim$80 ksec. The limiting source detection depths are 1.9×10^{-16} erg cm^{-2} s^{-1} in the Soft (0.5–2 keV) band, 7.3×10^{-16} erg cm^{-2} s^{-1} in the Hard (2–10 keV) band, and 5.7×10^{-16} erg cm^{-2} s^{-1} in the Full (0.5–10 keV) band. Here we describe the strategy, design and execution of the C-COSMOS survey, and present the catalog of 1761 point sources detected at a probability of being spurious of $<2 \times 10^{-5}$ (1655 in the Full, 1340 in the Soft, and 1017 in the Hard bands). By using a grid of 36 heavily ($\sim$50%) overlapping pointing positions with the ACIS-I imager, a remarkably uniform ($\pm$12%) exposure across the inner 0.5 sq.deg field was obtained, leading to a sharply defined lower flux limit. The widely different PSFs obtained in each exposure at each point in the field required a novel source detection method, because of the overlapping tiling strategy, which is described in a companion paper. This method produced reliable sources down to a 7–12 counts, as verified by the resulting logN-logS curve, with sub-arcsecond positions, enabling optical and infrared identifications of virtually all sources, as reported in a second companion paper. The full catalog is described here in detail and is available on-line.

Subject headings: surveys - catalogs - X-rays:general - cosmology:observations - (galaxies:) quasars: general - galaxies: evolution

1. Introduction

The co-evolution of galaxies and quasars or active galactic nuclei (AGNs) has been vigorously pursued both observationally and theoretically for a decade, ever since the discovery that the mass of the central black hole is tightly correlated both with the luminosity (Magorrian et al. 1998; Marconi & Hunt 2003) and the velocity dispersion of the spheroid (M_{BH}-σ relation; Ferrarese & Merrit 2000; Gebhardt et al. 2000; Tremaine et al. 2002). Tackling

[28]Research Center for Space and Cosmic Evolution, Ehime University, Bunkyo-cho 2-5, Matsuyama 790-8577, Japan

[29]Department of Astronomy, University of Michigan, Ann Arbor, MI 48109 USA

this large subject requires the study of both galaxies and AGNs back to the epoch when both were growing rapidly, i.e. z∼1-3, requiring deep observations across many wavelengths, from radio through the infrared, optical and ultraviolet, to the X-rays. At the same time, the wide range of cosmic density and the rapid changes in this large scale structure (LSS) require wide field observations that sample the Universe at close to their true fractions.

The Cosmic Evolution Survey (COSMOS, Scoville et al. 2007a) is a deep and wide extragalactic survey designed to have sufficient area to overcome most cosmic variance, which requires sampling regions some 50 Mpc on a side (Fig.1; Scoville et al. 2007a), and with sufficient depth to sample the $z = 1 - 3$ galaxy and AGN population. The contiguous 2 sq.deg COSMOS field samples a volume of $\sim 6 \times 10^6$ Mpc^3 at $z = 0.5 - 1$ (Wright 2006). This is $\sim 10\%$ of the volume imaged by the Sloan Digital Sky Survey (SDSS) in the local (z<0.1) universe (5.7×10^7Mpc^3, 8000 sq.deg, DR5[1]). COSMOS is a region of low, uniform, Galactic obscuration (E(B-V)≃0.02 mag, N_H (2.7×10^{20}cm^{-2}, Dickey & Lockman 1990). COSMOS is likely to be the largest survey of this type for the next decade.

The location of the COSMOS area near the equator (10^h, $+02°$) allows all major and future facilities[2] (notably EVLA, ALMA, and SKA) to target this region down to faint limits (Scoville et al. 2007a). Space-based imaging has been undertaken in the F840W ($\sim i$-band) with *Hubble Space Telescope* (HST, Scoville et al. 2007b), in the 3.5 μm-70μm infrared using *Spitzer* IRAC and MIPS (Sanders et al. 2007), in the UV using GALEX (Zamojski et al. 2007), and in 0.5-10 keV X-rays with XMM (Hasinger et al. 2007, Cappelluti et al. 2007). Ground-based imaging spans the radio (1400 MHz VLA, Schinnerer et al. 2007), the near-IR with CTIO and KPNO (Capak et al. 2007) and CFHT (McCracken et al. 2009, in preparation), the optical to AB∼26-27 with *Subaru* in 21 bands (Taniguchi et al. 2007). Finally, large dedicated ground-based spectroscopy programs in the optical with Magellan/IMACS (Trump et al. 2007), and VLT/VIMOS (Lilly et al. 2008) are well underway.

This wealth of data has resulted in an initial 15-band photometric catalog of $\sim 10^6$ objects (Capak et al. 2007) from which photometric redshifts good to <3% for z<1.2 and r <24 have been derived (Mobasher et al. 2007). Recently, more photometric bands have been added, resulting in improved photo-z's for the galaxy population accurate to Δz/(1+z)<1% (Ilbert et al. 2009) and to Δz/(1+z)∼2% for the AGN population (Salvato et al. 2009).

We have undertaken the *Chandra*-COSMOS survey (C-COSMOS) to cover the central

---
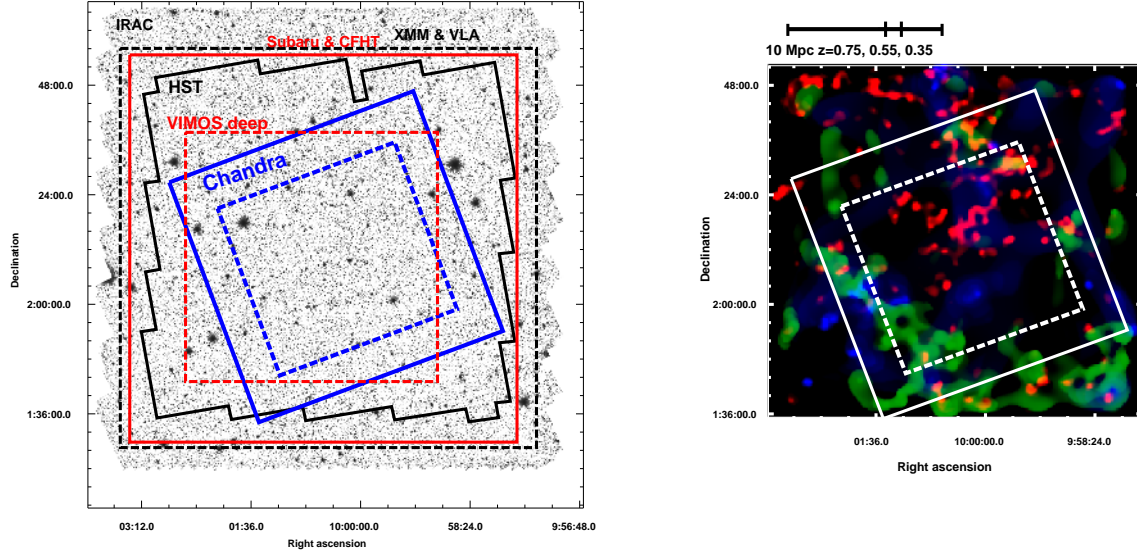
[1]URL: http://www.sdss.org/dr5/

[2]Except for those in Antartica.

Fig. 1.— *Left:* Map of the COSMOS field showing the coverage at various wavelengths: the IRAC 3.6μm mosaic is the background image; Blue solid=*Chandra*, blue dashed=*Chandra* deep; black polygon = HST; red solid = Subaru, CFHT, zCOSMOS bright; red dashed = zCOSMOS deep; black dashed = XMM and VLA. The *Spitzer* MIPS observations cover an area 2 times larger. *Right:* Large scale structure seen in galaxy distributions in the COSMOS field (Scoville et al. 2007c), ranging in size from 1 - 20 Mpc, based on photo-z's accurate to ∼1%. Blue is centered on z=0.35, Green on z=0.55, and Red on z=0.75, each with Δz=0.05. The C-COSMOS field outline is shown as the white tilted square, with the dashed line delineating the high exposure area as in the left panel. A scale showing 10 Mpc at the three redshifts is shown at the top. In both panels North is up, East is to the left.

0.9 sq.deg region of the COSMOS field (Fig.1, left), containing a wide range of cosmic overdensity (Fig.1, right), with the ACIS-I CCD imager (Garmire et al. 2003) on board the *Chandra X-ray Observatory* (Weisskopf et al. 2002). The survey took 1.8 Msec of *Chandra* observing time (∼21 days) and was the largest guest observer program approved in a single AO at the time it was undertaken (2006 November - 2007 June). C-COSMOS employed a series of 36 heavily overlapped ACIS-I 50 ksec pointings to give an exposure of ∼160 ksec over the inner area to a depth of $\sim 1.9 \times 10^{-16}$erg cm^{-2}s^{-1} (0.5-2 keV), providing an unprecedented combination of contiguous area and depth in the X-ray band. This overlapping tiling strategy gives highly uniform exposure, and so a well-defined flux limit.

Several of the deepest COSMOS surveys are now concentrating on this same central sub-field of COSMOS: the z-COSMOS Deep spectroscopic survey (to B∼25, Lilly et al. 2007), the deep VLA survey (6 μJy rms, Schinnerer et al. 2009, in preparation), and several

millimeter and sub-millimeter surveys (MAMBO, Bertoldi et al. 2007 and AzTEC, Scott et al. 2008). GALEX has observed the central field deeply (Zamojksi et al. 2007) and is currently monitoring this area. The Ultra-VISTA survey will undertake a deep yJHK survey of the central 1.5 sq.deg, half of which will be surveyed to the unprecedented limits of ∼26 AB mag (Arnaboldi et al. 2007).

By going for large area rather than extreme depth, most of the C-COSMOS sources are sufficiently bright to be detected in the rest of the pan-chromatic COSMOS data set, allowing rapid identifications (Civano et al. 2009) and determination of their multi-wavelength properties (e.g. Elvis et al. 2009, in preparation). On the other hand, C-COSMOS is sufficiently deep that significant numbers of normal and starburst galaxies with luminosity of 10^{42} erg s^{-1} can be detected up to $z \sim 0.9$, a redshift depth comparable with that of the galaxy redshift surveys in the COSMOS field (Taniguchi et al. 2007, Lilly et al. 2007). Adding the *Chandra* coverage to the COSMOS survey adds a valuable resource for the study of the co-evolution of black holes and their host galaxies, of the SEDs of faint quasars and active galactic nuclei, and the evolution of galaxies.

The summed image of the entire C-COSMOS field is shown in Fig.2 where colors have been mapped to X-ray bands.

This is the first of three papers presenting the basic results of the C-COSMOS survey over the whole field. Paper I (this paper) reports on the strategy, design and execution of the C-COSMOS survey, and present the catalog of 1761 point-like X-ray sources detected in C-COSMOS; Paper II (Puccetti et al. 2009) presents the details of the simulations carried out to optimize the source detection method; Paper III (Civano et al. 2009) presents the identification of the X-ray sources with optical and infrared counterparts. We conclude by listing the primary science objectives foreseen for the C-COSMOS data. Papers on several of these topics are in preparation.

We assume a ΛCDM cosmology with H$_0$=70 km s^{-1}, Ω_m=0.27, Ω_{vac}=0.73.

2. The Chandra COSMOS Strategy

For C-COSMOS we have developed a strategy that uses ∼50% overlapping tiling of the 16.9×16.9 arcmin ACIS-I fields. This tiling produces a remarkably uniform sensitivity in the central part of the field, and a well-defined flux limit with a sharp cut-off (Fig.3; for details on the generation of sensitivity maps see §7 in Paper II). This approach also ensures that the area with HPD<2″ is maximized, so that the unique *Chandra* high resolution imaging (van Speybroeck et al. 2002) can be exploited fully, albeit with 1/4 of the exposure time.
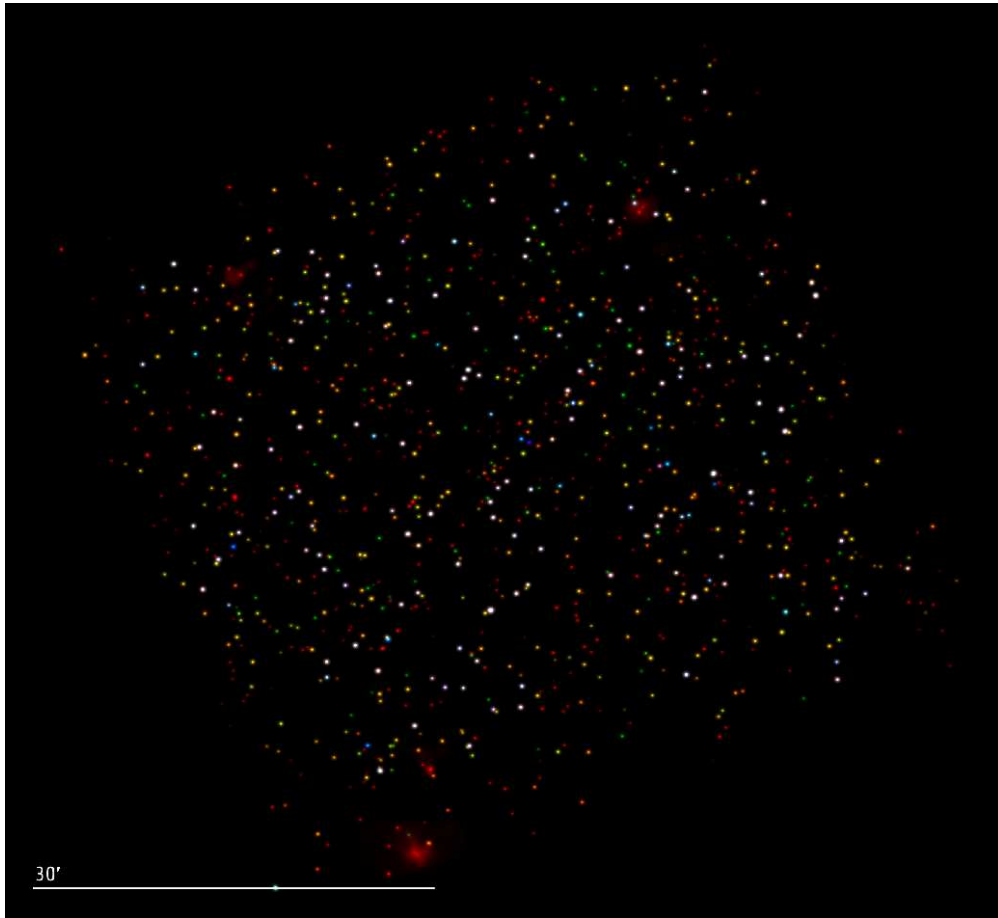
Fig. 2.— X-ray image of the Chandra COSMOS field, optimized to show point sources with a wide variety of X-ray colors. A scale showing 30 arcmin (the approximate diameter of the full moon) is shown for comparison. North is at the top; East is to the left. The full angular resolution of *Chandra* is not well represented in this image as, in order to display the point sources clearly, the original image has been smoothed with a sharp gaussian with radius equal to 2.9″, and added to an image of the field smoothed with a wide gaussian with radius equal to 4.4″. X-ray 'colors' are mapped so that red is the 0.5-2 keV band, green is the 2-4.5 keV band, Blue is the 4.5-7 keV band, and each energy band was smoothed in the same way. Selected prominent clusters have been adaptively smoothed for display (red extended shapes).

Table 1: C-COSMOS flux limits and corresponding XMM-COSMOS flux limits.

Band	C-COSMOS(lim)[a]	C-COSMOS(logN-logS)[a]	XMM-COSMOS[a]
Soft (0.5–2 keV)	1.9	2.5	5
Hard (2–10 keV)	7.3	16	25
Full (0.5–10 keV)	5.7	—	—

[a] flux limits are reported in units of 10^{-16}erg cm^{-2}s^{-1}, for bands up to 10 keV, but were measured only up to 7 keV. (See text for details.)

The good *Chandra* point spread function (PSF) resolves sources $2''$ apart over $\sim$0.7 sq.deg, corresponding to 8-16 kpc separations for z=0.3-0.9, and locates point sources to <4 kpc at *any redshift*. Thus close mergers can be resolved, and nuclear sources distinguished from off-nuclear sources in galaxies (Ultra-luminous X-ray Sources, ULXs, Fabbiano 2006, Lehmer et al. 2006, Mainieri et al. 2009, in preparation).

Point source detection sensitivities were estimated for three standard *Chandra* bands: Soft (S, 0.5-2 keV), Hard (H, 2-10 keV) and Full (F, 0.5–10 keV). Due to the high background in the 7-10 keV energy range[3], channels above 7 keV were not used for source detection. (See §4.2.2 and Paper II for details). The C-COSMOS flux limits in 3 bands are reported in Table 1, together with the XMM-COSMOS limits for comparison: C-COSMOS sensitivity is three times below the corresponding flux limits for the XMM-COSMOS survey (dashed line; Cappelluti et al. 2009), making them complementary surveys.

The achieved sensitivity-area curve[4](Fig. 3) has a sharp cut-off at low fluxes.

The C-COSMOS Soft band flux limit corresponds to luminosities of (0.8, 4, 11)$\times 10^{41}$erg s^{-1} at z=(0.3, 0.6, 0.9) respectively, while the Hard band flux limit corresponds to four times higher luminosities. Both luminous elliptical galaxies and starbursts often exceed these luminosities, and starburst galaxies are known to become common (Hornschemeier et al. 2003) at these X-ray fluxes.

The low ACIS background enables stacking analysis, in which counts at the positions of known classes of objects, e.g. subsets of the thousands of galaxies with redshifts, are co-added to increase the effective exposure time (Brusa et al. 2002; Hornschemeier et al. 2002; Brandt et al. 2001; Nandra et al. 2002; Fiore et al. 2008a,b).

---

[3]URL: http://cxc.harvard.edu/contrib/maxim/bg/index.html#spec

[4]This curve is remarkably close to the predictions from the proposal, reflecting the high accuracy with which the requested tiling was executed.
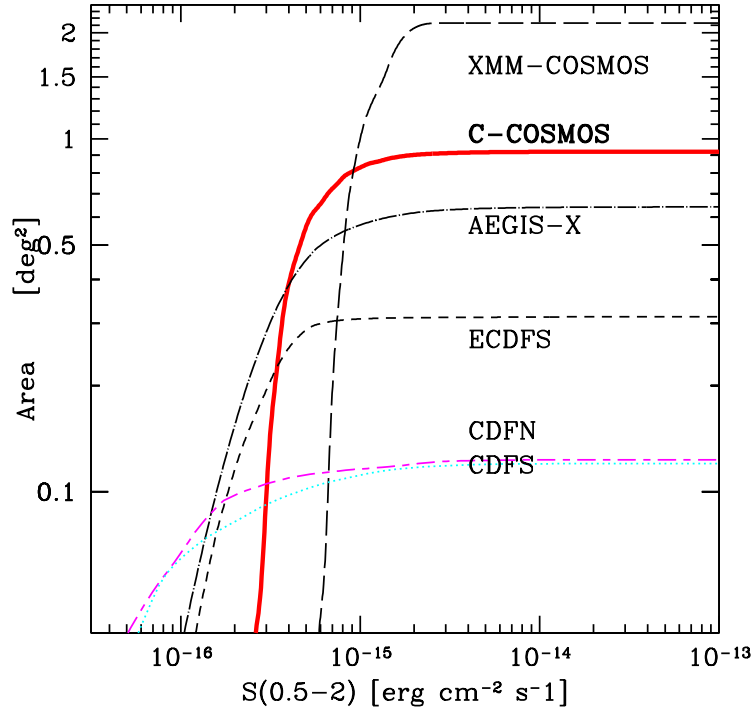
Fig. 3.— Area-flux curve for C-COSMOS (red solid line, 0.5-2 keV). The coverage of ECDFS (Lehmer et al. 2005; dashed line), AEGIS-X (Laird et al. 2008; dash-dotted line), CDFN (Alexander et al. 2003; magenta short-long dashed line), CDFS (Luo et al. 2008; cyan dotted line) and XMM-COSMOS (Cappelluti et al. 2009; black dashed line) are shown for comparison.

2.1.   Design

The C-COSMOS tiling scheme (Fig. 4, left panel) covers the central area of the COS-MOS field in the most efficient manner that we could devise. A 6×6 raster array of 36 ACIS-I pointings (one ACIS pointing field of view is outlined in black in Fig. 4, *left*), each of 50 ksec nominal exposure, were chosen. The center of the array (Table 2) is slightly offset from the center of the COSMOS field to match the z-COSMOS deep field (Lilly et al. 2007).

The value of the 8.0′ offset between pointing centers was chosen to be slightly less than the 8.3′ size of an ACIS chip (Garmire et al., 2003, Chandra Proposers' Observatory Guide, aka POG, 2007[5]) Table 6.1), so that chip gaps are not co-added to create small scale dips in the effective exposure time.

The inner part of the field was covered by four exposures, to give a total nominal exposure of 200 ksec (effective exposure ∼160 ksec) over a 42′×42′ area (0.5 sq.deg,green area in Fig. 4). The outer region has been covered by two observations (blue area) and the four corners covered by 1 observation (purple area). The corners of the outer and inner regions are reported in Table 2 clockwise from the top left.

Sources at a flux of ∼2.0×10^{-16}erg cm^{-2}s^{-1} (0.5-2 keV) have a total of 5–10 summed counts in the four exposures, ensuring a good detection, given the low *Chandra*/ACIS background of ∼2 counts/200 ksec over a 2 arcsec radius circle (see §4.2.1).

The heavily overlapped tiling scheme produces a smooth exposure map that is flat to 12% in the central region (see Figure 4, right panel and §4.2.2).

2.2.   Comparison with Other Legacy Surveys

Chandra observing time has been dedicated to several large legacy surveys: CDF-S (Giacconi et al. 2002; Luo et al. 2008), CDF-N (Alexander et al. 2003), ECDF-S (Lehmer et al. 2005), AEGIS-X (Nandra et al. 2005; Laird et al. 2008), XBootes (Murray et al. 2005). These surveys have different emphases in area and depth, so we summarize the special features of C-COSMOS here.

Like all contiguous area surveys, C-COSMOS has significant advantages over non-contiguous surveys (e.g. SEXSI, Harrison et al. 2003, Eckart et al. 2006; ChaMP, Kim et al.

---

[5]Chandra X-ray Center publication TD 403.00.010

Table 2: Coordinates of the C-COSMOS field, center and corners of the outer and inner regions, clockwise from the NE (top left).

	RA	Dec
Center		
	10^h 00^m 24^s	$+02° \ 10' \ 55''$
Outer region		
	10^h 02^m 45^s	$+02° \ 26' \ 47''$
	09^h 59^m 11^s	$+02° \ 46' \ 45''$
	09^h 57^m 54^s	$+01° \ 53' \ 00''$
	10^h 01^m 23^s	$+01° \ 33' \ 59''$
Inner region		
	10^h 02^m 05^s	$+02° \ 21' \ 13''$
	09^h 59^m 30^s	$+02° \ 35' \ 47''$
	09^h 58^m 35^s	$+01° \ 59' \ 19''$
	10^h 01^m 11^s	$+01° \ 44' \ 37''$

2007), because of the difficulty of getting deep multi-wavelength coverage of non-contiguous fields.

C-COSMOS is neither the deepest (CDFN and CDFS) nor the widest (XBootes) legacy *Chandra* survey. A comparable sensitivity has been reached in the somewhat smaller AEGIS field (dot-dashed line in Fig. 3; Laird et al. 2008). C-COSMOS differs from the other surveys by having the largest area at fluxes $0.3 - 1 \times 10^{-15}$erg cm^{-2}s^{-1}, and a sharper low flux limit cut-off in the area surveyed than most other recent X-ray surveys. The single field CDF-S and CDF-N have notably shallower roll-offs in their sensitivity curves (magenta and blue lines in Fig. 3).

Hence, to compare the area and depth of C-COSMOS with comparable contiguous *Chandra* and *XMM-Newton* surveys in a consistent fashion requires a slightly revised measure of area and depth. We have used the Area-Flux plot from each survey to derive the flux at the point where each survey reaches 80% of the maximum survey area. We plot these values in Figure 5 (filled circles) for the *Chandra* contiguous area surveys (CDFN, Alexander et al. 2003; CDFS, Luo et al. 2008; ECDFS, Lehmer et al. 2005; AEGIS- X, Laird et al. 2008; XBootes, Murray et al. 2005; ELAIS-N, Manners et al. 2003), and for the *XMM-Newton* contiguous surveys that fill regions of the flux-area plane (ELAIS-S1, Puccetti et al. 2006; XMM-COSMOS, Cappelluti et al. 2009; Lockman-Hole, Brunner et al. 2008). The C-COSMOS flux at 80% of the area covered (0.72 sq.deg) in the Soft band is 6×10^{-16}erg cm^{-2}s^{-1}.

Compared with other plots of this kind (e.g. Brandt & Hasinger 2005) survey points in Figure 5 tend to be moved diagonally toward smaller area and high flux limits. This shift
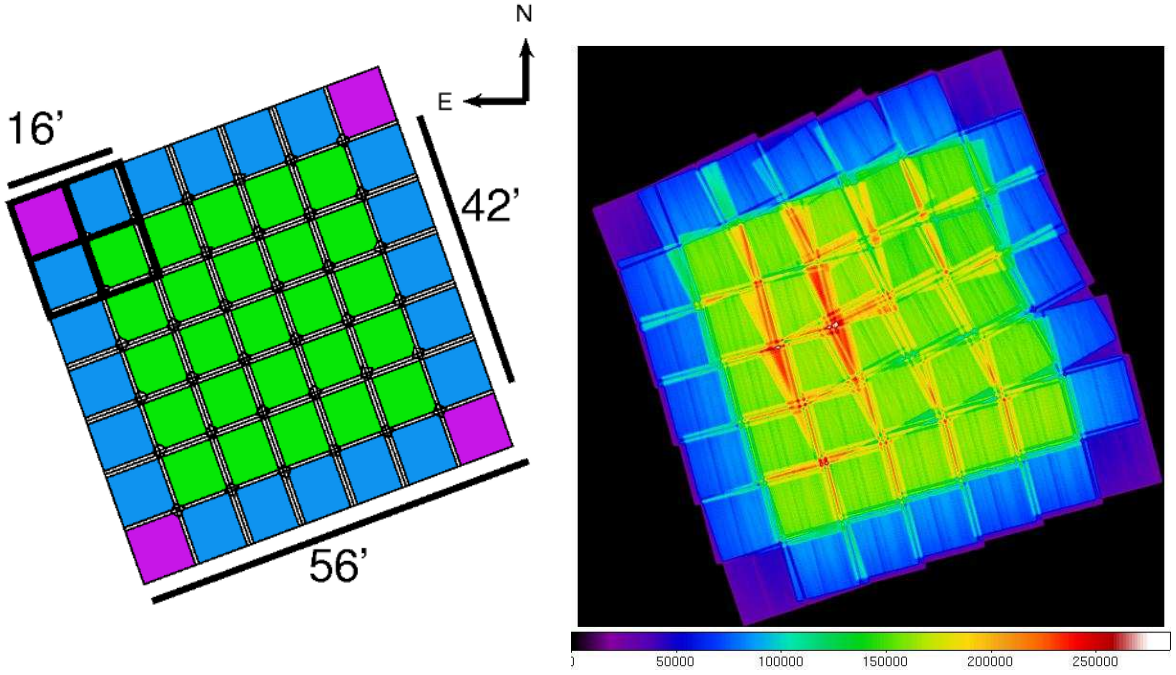
Fig. 4.— *Left:* The 'as designed' C-COSMOS tiling for the 36 50 ksec pointings. The thick black box (top left) represents one ACIS-I pointing, the thin boxes all the pointings. Different colors show areas with different number of overlapping pointings: green - 4 overlapping pointings; blue - 2 overlapping pointings; purple - 1 pointing. The black bars show roughly the relative dimensions of one pointing ($\sim$16′), of the inner area with larger exposure ($\sim$42′), and of the total field ($\sim$56′). Raster point (see Table 3 1-1 lies at the top right (NE) and 1-6 lies at the top-left (NW). *Right:* The 'as executed' exposure map for the C-COSMOS survey in the Soft band. The color bar gives the achieved effective exposure in units of seconds.

can be quite large for surveys with shallow slopes at low fluxes in their area-flux limit curves (as for examples the deep fields). This is because the normally quoted area is the maximum area of the survey, while the normally quoted flux limit is that of the faintest source in the survey, which can be detected only in a much smaller area.

Curves of constant numbers of sources (for the Soft band) are shown in Fig. 5 following the predictions of Gilli et al. (2007) XRB model[6]. The larger numbers in XBootes and the two COSMOS surveys are notable. Some 1000 sources are predicted for C-COSMOS above the '80% area' flux limit in the Soft band based on the logN-logS relation of Gilli et al.

---

[6]The curves have been computed using the tool "POrtable Multi Purpose Application for XRB and AGN counts" available at the web site http://www.bo.astro.it/$\sim$gilli/counts.html.

(2007), while 1023 are actually detected. This can be compared with the CDF fields which have ∼200 sources each.

A single number does not convey the complete picture, of course. We also show in Fig.5 the Area-Flux curve of each survey down to 20% of the area. These curves better explain the differences between the surveys, notably between the two CDF deep fields, that are due to the different observation's strategy [changing only the roll angle (CDF-N) or also moving the centroid (CDF-S)]. The more sensitive, smaller area, parts of each survey add more sources than indicated by the dashed black lines, especially for the curves that are closer to vertical. For example, the AEGIS-X survey (Laird et al. 2009) has 1032 soft sources, about double the number predicted at the 80% point. C-COSMOS, with a flatter flux-area curve, has a total of 1340 S band sources, ∼30% higher than the 80% area number.

Each of these surveys has extended multi-wavelength coverage, but C-COSMOS is the only deep and wide X-ray survey field selected for both existing deep multi-wavelength coverage, and for future legacy value, due to the equatorial location of the COSMOS field. The AEGIS field (δ=+52°), the CDF-N field (δ=+62°) and the XBootes field (δ=+35°) are all too northerly to be accessible by ALMA or the VLT. The COSMOS field was also selected to have low IR cirrus emission, and a lack of bright stars, X-ray or radio sources in the field to maximize multi-wavelength coverage.

C-COSMOS and XMM-COSMOS complement one another by providing large samples of sources over a wide flux range (Fig. 8), while sharing the same extensive multi-wavelength data set. XMM-COSMOS provides a larger sample of extended sources, while C-COSMOS provides a larger sample of starburst and normal galaxies.

3. Observations

A summary of the *Chandra* ACIS-I C-COSMOS observations as carried out is given in Table 3. Primarily because of thermal constraints on spacecraft components (POG, §3.3.3), many of the 36 C-COSMOS pointings were scheduled as two or more separate ObsIDs, giving 49 C-COSMOS observations in all. The indices X-Y (1-1 through 6-6) describe the field numbers, where X is an index in RA and Y an index in Dec, with 1-1 being in the top right (NE) corner of Fig. 4 (left panel), and 1-6 being in the top left (NW) corner.

The observations took place in two main blocks: 2006 December - 2007 Jan and 2007 April-June (Table 3). The fields were observed at nominal roll angles of 250/70 deg, where the visibility of the COSMOS field is at maximum (∼70%) and the pitch angle is such that the constraints are either unrestricted or restricted only to avoid overheating of the charged
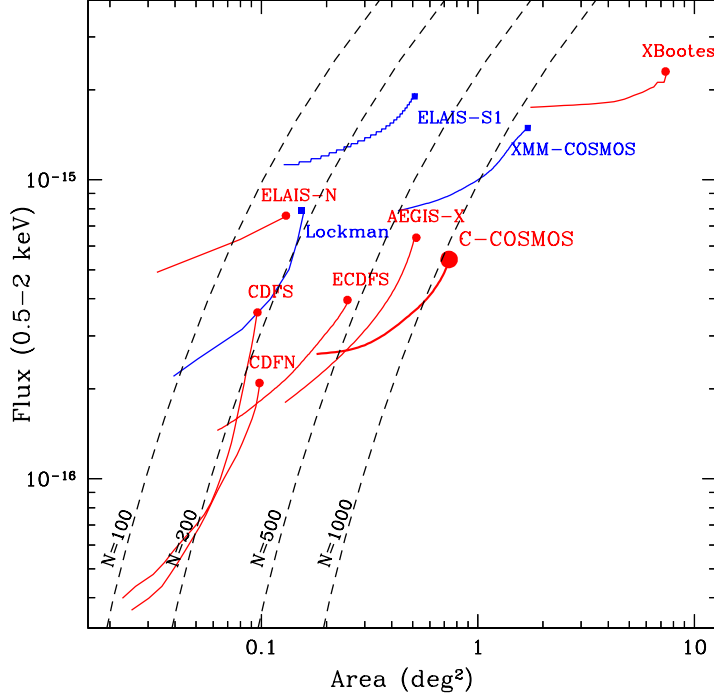
Fig. 5.— Area-Flux curves for *Chandra* (red) and *XMM-Newton* (blue) contiguous X-ray surveys. Each survey has been plotted using each sensitivity curve starting from the flux corresponding to the area that is 80% of the maximum area for that survey (large points at the top of each curve), to the flux corresponding to the 20% of the total area (bottom of each curve). Data were taken from the following *Chandra* references: XBootes - Murray et al. 2005; CDFN - Alexander et al. 2003; CDFS - Luo et al. 2008; ECDFS - Lehmer et al. 2005; AEGIS-X - Laird et al. 2008; ELAIS-N - Manners et al. 2003; and XMM-Newton references: XMM-COSMOS - Cappelluti et al. 2009; Lockman - Brunner et al. 2008; ELAIS-S - Puccetti et al. 2006. The black dashed curves show the total number of 0.5-2 keV sources expected based on the logN-logS relation predicted by Gilli et al. (2007) at the 80% area point.

particle detector (EPHIN). As an equatorial field, the roll angle of the COSMOS field is quite stable (55.2–69.6, 248.4–256.2) for periods of $\sim$100 days. As a result, the *Chandra X-ray Center* (CXC) Mission Planning team were able to maintain a tight roll angle range of $\pm 6°$ around the nominal values (Table 3), leading to a highly uniform exposure of the whole field.

The mean effective exposure time per field (not per ObsID) is 46.3 ksec, when only the Good Time Intervals (GTIs), cleaned of the few high background times (§4.2.1) are used[7]. The maximum exposure is 48.3 ksec and the minimum exposure (excluding a single 37.6 ksec exposure for field 2-5, Table 3) is 44.1 ksec. So, with this exception, the range of exposures over the fully covered inner region varies by just ± 2.0 ksec (4%).

4. Data Processing

The data from the 49 obsids were uniformly processed in two phases using the CIAO 3.4 software tools[8] (Fruscione et al. 2006) , the *yaxx*[9] tool and custom versions of the XMM SAS detect tool EMLDETECT[10]. Standard Level-1 and Level-2 processing pipeline[11] (AS-CDS version 7.6.9) from the CXC were used. In the first processing phase we determined astrometric corrections (see below) for each ObsID. These corrections were then applied in the second phase where we reprocessed all event data starting with Level-1 products.

Data processing involved the following series of steps, as summarized below:

1. Astrometric corrections ($<1.1''$) to the standard COSMOS frame starting with the CXC supplied standard data products (§6);

2. Baseline data product creation by re-processing all ObsIDs to a standard frame of reference using the new astrometry and standard CXC pipelines (§4.2);

---

[7]This is $\sim$93% of the requested exposure, well within the 90% tolerance limit defined for *Chandra* scheduling.

[8]URLhttp://cxc.harvard.edu/ciao/

[9]http://cxc.harvard.edu/contrib/yaxx/

[10]http://xmm.esac.esa.int/sas/8.0.0/EMLdetect

[11]Pipeline processing levels are explained at URL: http://cxc.harvard.edu/ciao/data/sdp.html

Table 3: *Chandra-COSMOS observation summary*

Obs. ID	Field	Obs. Start (UT)	Exp. Time[a] (ks)	RA (J2000.0)	Dec (J2000.0)	Roll (deg)
7995	1-1	2007 Jun 01, 03:41	44.6	10 02 02.05	+02 22 36.46	248.4
7996	1-2	2006 Dec 28, 11:28	44.7	10 01 31.99	+02 25 20.48	63.4
7997	1-3	2006 Dec 30, 21:10	44.5	10 01 01.92	+02 28 04.50	62.8
8494	1-4	2006 Dec 16, 13:21	20.2	10 00 31.85	+02 30 48.52	66.4
8122	1-4	2007 Jan 20, 10:15	28.0	10 00 31.85	+02 30 48.52	55.2
8493	1-5	2006 Dec 12, 18:07	19.3	10 00 01.79	+02 33 32.55	66.4
7998	1-5	2007 Jan 10, 21:41	26.9	10 00 01.79	+02 33 32.55	63.2
8478	1-6	2006 Nov 24, 10:17	17.6	09 59 31.72	+02 36 16.58	69.6
7999	1-6	2006 Nov 25, 09:24	29.0	09 59 31.72	+02 36 16.58	69.6
8000	2-1	2007 May 26, 20:23	45.2	10 01 51.10	+02 15 05.52	253.2
8001	2-2	2007 Apr 02, 03:42	47.3	10 01 21.03	+02 17 49.54	256.2
8123	2-3	2007 Apr 07, 13:40	48.3	10 00 50.97	+02 20 33.55	255.2
8002	2-4	2006 Dec 19, 04:57	28.5	10 00 20.90	+02 23 17.58	65.0
8496	2-4	2006 Dec 23, 12:05	17.8	10 00 20.90	+02 23 17.58	65.0
8003	2-5	2007 Apr 02, 17:53	37.6	09 59 50.83	+02 26 01.61	255.2
8004	2-6	2006 Nov 27, 02:25	15.3	09 59 20.76	+02 28 45.64	68.6
8482	2-6	2006 Dec 02, 09:05	10.2	09 59 20.76	+02 28 45.64	68.6
8483	2-6	2006 Dec 04, 03:02	21.3	09 59 20.76	+02 28 45.64	68.6
8005	3-1	2007 Apr 25, 02:42	30.8	10 01 40.15	+02 07 34.57	255.2
8552	3-1	2007 Apr 26, 09:33	14.4	10 01 40.15	+02 07 34.57	255.2
8124	3-2	2007 Apr 08, 03:42	31.1	10 01 10.08	+02 10 18.59	255.2
8549	3-2	2007 May 05, 17:17	17.2	10 01 10.08	+02 10 18.59	255.2
8503	3-3	2006 Dec 31, 10:18	20.0	10 00 40.02	+02 13 02.61	62.2
8006	3-3	2007 Jan 01, 11:48	25.8	10 00 40.02	+02 13 02.61	62.2
8007	3-4	2006 Dec 19, 22:18	21.1	10 00 09.95	+02 15 46.64	64.2
8497	3-4	2006 Dec 25, 01:50	27.1	10 00 09.95	+02 15 46.64	64.2
8008	3-5	2007 Jan 02, 04:39	45.0	09 59 39.88	+02 18 30.67	61.9
8009	3-6	2007 Jan 02, 18:06	44.8	09 59 09.81	+02 21 14.70	61.8
8010	4-1	2007 Apr 27, 18:45	32.9	10 01 29.19	+02 00 03.29	255.2
8553	4-1	2007 Apr 29, 01:02	14.4	10 01 29.19	+02 00 03.29	255.2
8011	4-2	2007 Apr 04, 04:08	45.8	10 00 59.13	+02 02 47.30	255.2
8012	4-3	2007 Jan 04, 05:30	48.0	10 00 29.06	+02 05 31.33	61.3
8013	4-4	2007 Jan 04, 19:44	46.9	09 59 58.99	+02 08 15.36	61.1
8014	4-5	2007 Jan 05, 09:29	44.2	09 59 28.92	+02 10 59.38	60.9
8015	4-6	2007 Jan 07, 09:53	44.1	09 58 58.85	+02 13 43.42	60.2
8550	5-1	2007 Apr 18, 19:11	22.7	10 01 18.25	+01 52 32.34	255.2
8016	5-1	2007 Apr 19, 20:24	23.3	10 01 18.25	+01 52 32.34	255.2
8017	5-2	2007 Apr 04, 17:55	45.3	10 00 48.18	+01 55 16.35	255.2
8018	5-3	2007 Apr 05, 07:17	45.8	10 00 18.11	+01 58 00.38	255.2
8019	5-4	2007 Apr 06, 23:25	48.0	09 59 48.04	+02 00 44.41	255.2
8020	5-5	2007 Apr 09, 06:12	47.8	09 59 17.97	+02 03 28.44	255.2
8021	5-6	2007 Apr 09, 20:24	47.3	09 58 47.90	+02 06 12.48	255.2
8022	6-1	2007 May 10, 23:28	30.9	10 01 07.30	+01 45 01.39	251.4
8555	6-1	2007 May 12, 16:06	16.2	10 01 07.30	+01 45 01.39	251.4
8023	6-2	2007 Apr 10, 12:49	48.3	10 00 37.24	+01 47 45.41	255.2
8024	6-3	2007 Apr 11, 21:40	47.9	10 00 07.17	+01 50 29.44	255.2
8025	6-4	2007 Apr 12, 11:57	47.9	09 59 37.10	+01 53 13.47	255.2
8026	6-5	2007 Apr 13, 07:31	45.8	09 59 07.03	+01 55 57.49	255.2
8027	6-6	2007 Apr 14, 13:54	48.3	09 58 36.96	+01 58 41.53	255.2

[a]After GTI and high-background filtering for two affected obsids. Intervals of 8.50 ksec and 2.45 ksec (respectively) were eliminated from the two affected ObsIDs (8003, 8014).

3. Background reduction using high background time filtering (which affects only two ObsIDs) (§4.2.1);

4. Exposure map creation in the three energy bands F, S, and H, using the standard CIAO tool sequence (§4.2.2);

5. Calculation of the sky coverage (i.e. the area covered to a given flux threshold) in the three energy bands, F, S and H;

6. Candidate source detection using a wavelet technique (PWDetect, Damiani et al. 1997)[12];

7. Selection of reliable sources, with a probability of being spurious $<2\times10^{-5}$ in at least one band, using maximum likelihood fitting (EMLdetect) applied *simultaneously to each ObsID* at the positions of all candidate sources; Puccetti et al. (Paper II) shows that EMLdetect reconstructs the input count rate of simulations well, while both PWDetect and detector underestimate the input count rate by about 15%;

8. Reliability checks for all sources using simulations, searches for outliers and visual checks (rejected candidate sources were all in the wings of bright source PSFs);

9. Aperture photometry of reliable sources. At high fluxes the systematic error in the PSF, which is intrinsic to the EMLdetect method, becomes larger than the statistical error; this systematic error is not present for aperture photometry.

10. Derivation of reliability and completeness criteria for the source catalog, leading to a logN-logS curve that provides an end-to-end check of the source extraction by comparing with other surveys in the same flux range (§9).

Steps 1 to 4 are discussed more fully in the following subsections. Complete details of the steps from 5 onwards, including details of the simulations and tests, are given in Paper II.

4.1. Astrometry corrections

In the first phase we determined accurate astrometric offsets for each ObsID. The good absolute astrometry produced by *Chandra* (0.6″ at 90% confidence, POG, §5) is still of the

---

[12] We compared PWDetect with the CIAO tool wavdetect used by most *Chandra* deep surveys on a subset of C-COSMOS fields, and found no substantive difference in the results; PWDetect is a much faster algorithm, due to better memory buffering.

order of one ACIS pixel. To avoid a loss of sensitivity, correcting the astrometry to much less than one pixel error is needed before merging event files, or stacking.

To this end, we first produced a list of bright X-ray sources for each of the 49 ObsIDs, using the standard CIAO CELLDETECT tool. Starting with the standard ACIS Level-2 data products, we generated a broad-band exposure map for each ACIS CCD using the CIAO[13] tools ASPHIST, MKINSTMAP, and MKEXPMAP. These exposure maps and event files were then used as input to a *Chandra*-adapted version of the XMM-SAS tool EMLDETECT (see next section), with an input source candidate catalog obtained by running the sliding cell detection tool EBOXDETECT with a high threshold. All sources detected with likelihood parameter $\mathcal{L} > 10$ were compared with the CFHT MegaCam I-band catalog of the COSMOS field (Capak et al. 2007), selecting only the point-like sources with I magnitudes in the range 18–23. Using this restricted magnitude range minimizes systematic effects introduced by bright stars (saturation) and faint background objects (misidentification), and is appropriate for sources in this flux range (Brandt & Hasinger 2005). An optical–X-ray position correlation was computed using the likelihood algorithm included in the SAS task EPOSCORR (Cappelluti et al. 2007, 2009). This task uses all the possible counterparts of an X-ray source in the field to determine the most likely coordinate displacement. This method is independent of the actual spectroscopic identifications, but *post facto* all the identifications have proved to be correct (Paper III). No statistically significant offset in roll was required for any ObsID, so the change in roll was set to exactly zero. The systematic offsets between the X-ray and the optical positions were always smaller than 1.1 arcsec, with an average shift of ΔRA= $0.04''$ and Δdec=$0.25''$.

4.2. Baseline Data Products

The second phase of processing brought the 49 *Chandra* ObsIDs to a common reference frame using the offsets derived above, and generated the baseline data products that were then used as the starting point in all subsequent C-COSMOS analysis.

This processing was based on the CIAO thread for creating a new Level-2 event file from Level-1 products[14]. First, a new aspect solution for each ObsID was generated to remove the astrometric offset for each ObsID derived in above section, using the REPROJECT_ASPECT tool. Then a new bad pixel file was created using ACIS_RUN_HOTPIX (see 'background reduc-

---

[13]URL: http://cxc.harvard.edu/ciao/
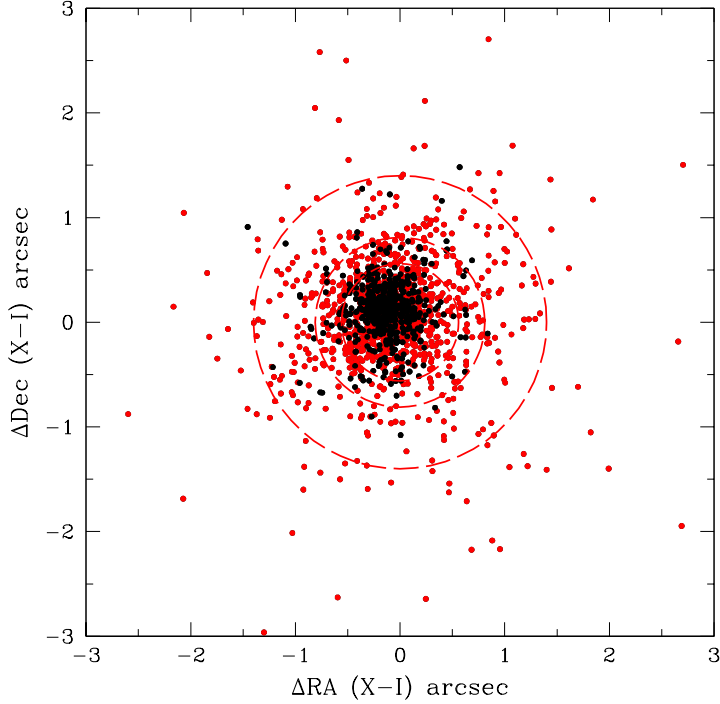
[14]http://cxc.harvard.edu/ciao3.4/threads/createL2/

Fig. 6.— The X-ray to I-band offsets (ΔRA, Δdec) in arcsec for X-ray sources with a secure identification (Civano et al. 2009) after the aspect correction described in the text has been applied (§4.1). The circles encompass 68% (0.56″), 90% (0.81″) and 95% (1.41″) of the sources with optical counterparts and secure identification. Red dots mark sources with less than 50 counts in the Full band.

tion' below). Finally, a new ACIS Level-2 event file was then created for each ObsID using the ACIS_PROCESS_EVENTS tool, with: (a) the standard *ASCA* grade set (grades [0, 2, 3, 4, and 6], POG §6.14), (b) pixel randomization turned off, (c) PHA randomization turned on, (d) Very-Faint mode processing enabled, and (e) the new aspect solution applied.

The astrometric corrections were checked using X-ray sources with point-like optical counterparts (Civano et al. 2009, Paper III) that were *not* used to derive the offsets for the individual ObsIDs. The residual systematic shift (X-ray – Optical position) is on average $\Delta\alpha$= -0.1″ and Δdec=0.08″, and the 1 σ dispersion is 0.56″ (i.e. the radius within which 68% of sources lie; Fig. 6). We find that 90% of the X-ray positions agree with the identified optical/IR counterpart positions to within 1.1″. The residual systematic shift is small enough that it will not affect the identification of any individual source and is smaller than the average X-ray positional error, and therefore has not been used to correct the astrometry any further. The good quality of the data provides positions with sub-arcsecond accuracy at

off-axis angle $<6'$, in agreement with other *Chandra* surveys (0.23-1.90$''$ in the CDFS, Luo et al. 2008; 0.3-1.67$''$ in AEGIS, Laird et al. 2008).

4.2.1.   Background reduction and cosmic ray afterglow detection

Intervals of high background were determined by creating a background light curve for the ACIS-I CCD events with point sources found by WAVDETECT in the phase 1 processing removed. Only two obsids showed intervals with a significant ($> 5\text{-}\sigma$) deviation from the quiescent background level (see Table 3).

Particular care was taken in the rejection of cosmic-ray afterglows[15].   When a cosmic ray hits a CCD pixel a residual charge can remain localized for tens of seconds and produce "afterglow events", that appear to be X-ray events, at one location for several consecutive CCD frame readouts (POG §6.9). To reject cosmic ray afterglows we used the CIAO tool ACIS_RUN_HOTPIX[16] and enabled Very-Faint (VF) mode background processing in ACIS_PROCESS_EVENTS. This process was successful as none of the C-COSMOS sources subsequently detected have the time localization characteristic of a spurious afterglow source. This procedure also gave a 25-30% background reduction in the 0.5-7 keV band.

The residual background is very stable over the full field of view at $\sim 1.8 \times 10^{-7}$ counts/s/pixel or $\sim$2 counts/200 ksec over a 2 arcsec radius circle, which represents the typical size of our detection cell across the field. Following Alexander et al. (2003), in which the transition between a photon limited and a background limited regime is defined as >3.3 background counts per detection cell for S/N=3, we conclude that C-COSMOS is photon limited for point source detection.

4.2.2.   Exposure Maps and Sensitivity Curve

We constructed exposure maps using the standard CIAO tool sequence of ASPHIST, MKINSTMAP, and MKEXPMAP, for each ObsID on a per-CCD basis, in each of three energy bands, S, H, F.

Figure 4 (right panel) shows a composite image of the effective exposure time (sec) in the Soft band. We clearly see the central region with four overlapping pointings, the side

---

[15]URL: http://cxc.harvard.edu/ciao/why/afterglows.html

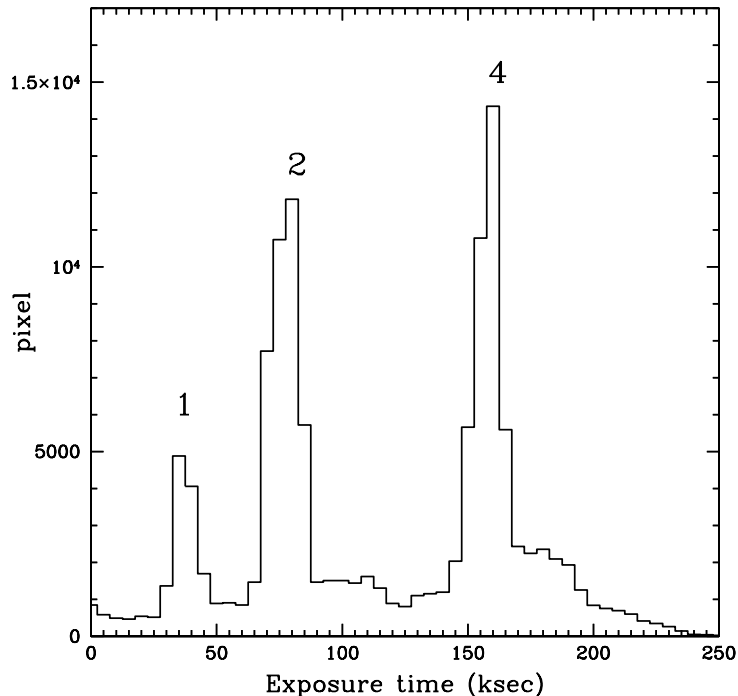[16]http://cxc.harvard.edu/ciao3.4/ahelp/acis_run_hotpix.html

Fig. 7.— Histogram of the exposure times in the summed C-COSMOS field. The narrow peaks lie at the 1, 2 and 4 exposure values. The broader bases correspond to overlaps caused by slight variations in the roll angles of the ObsIDs.

strips with two observations, and the corners covered by just one pointing. The uniformity of the exposure in the central region is shown by the histogram of the exposure times shown in Fig.7. This histogram shows narrow peaks at the 1, 2 and 4 exposure values, which have gaussian sigmas of 12.9, 13.6 and 19.3 ksec, respectively, i.e. a 12% spread on the central region exposure. The total effective exposure in the inner, 4 exposure, region is $\sim$160 ksec at the peak, and $\sim$170 ksec at the mean, in the same region (see Fig. 7).

The C-COSMOS sky coverage (i.e. the area covered as a function of limiting sensitivity) was computed in the three standard energy bands, F, S, H using the exposure maps, the background maps and assuming a spectrum with $\Gamma = 1.4$ and $N_H = N_H$(Galactic). The sky coverage in the Soft band is shown in Fig. 3. More details on the Full band and Hard band are given in Paper II (§7).

The main uncertainty in the estimated sky coverage comes from the range of conversion factors from count rates to fluxes induced by the variety of intrinsic X-ray spectra in the X-ray population, in both power-law slope and intrinsic absorption, at a minimum. More

Table 4: Conversion factors from count rates in the Soft, Full and Hard bands (0.5-2, 0.5-7, 2-7 keV) to fluxes in the same bands for different spectral assumptions[a], computed with the *Chandra* Cycle 8 response matrices.

Γ	N_H	factor[b]
	cm^{-2}	
Soft Band		
1.4	Galactic	1.87
1.7	Galactic	1.81
2.0	Galactic	1.75
1.4	10^{22}	2.12
2.0	10^{22}	2.15
Full Band		
1.4	Galactic	0.75
1.7	Galactic	0.89
2.0	Galactic	1.04
1.4	10^{22}	0.51
2.0	10^{22}	0.71
Hard Band		
1.4	Galactic	0.38
1.7	Galactic	0.43
2.0	Galactic	0.47
1.4	10^{22}	0.36
2.0	10^{22}	0.45

[a] Γ=1.4, N_H=Galactic used for catalog fluxes.
[b] conversion factor CF where $Flux = B_{rate}/(CF * 10^{11})$, in units of $cts\ erg^{-1}\ cm^2$.

complex spectra are surely present. An additional complication is that the average spectral properties are a function of the observed flux (Brandt & Hasinger 2005). To estimate this uncertainty, we calculated the sky coverage for power law spectra with Γ =1.4 and 2.0 with Galactic N_H, and for absorbed power law spectra with Γ =1.4 and 2.0 and $N_H = 10^{22}$ cm^{-2}. The range of conversion factors, given by PIMMS[17] is a factor 2.0 in the F band, 1.3 in the H band and 1.2 in the S band (Table 4). As expected from the large width of the Full band, the uncertainty for the Full band is larger than for the Soft and Hard bands.

---

[17]URL: http://http://cxc.harvard.edu/toolkit/pimms.jsp

5. Point Source Catalog

5.1. Overview

In this catalog we report the 1761 sources detected down to a defined threshold in at least one band. The threshold was chosen to balance completeness (the fraction of true sources detected) against reliability (the fraction of false sources detected). Paper II describes simulations that allowed us to choose a threshold which has a known completeness and reliability. We chose a probability threshold of P=2×10^{-5}, giving 99.8% reliability for sources with more than 12 counts and 99.7% reliability for sources with 7 counts. This implies $\sim$3-5 spurious F band detections in the full field with > 12 counts and 5 spurious detections with > 7. At this threshold, the simulations then show that C-COSMOS is 87.5% complete for 12 count sources and 68% complete for 7 count sources. The C-COSMOS false source rates are consistent with those of other surveys (e.g. AEGIS-X, Laird et al. 2008) once the higher C-COSMOS threshold and larger average source extraction region are taken into account (see Paper II, §6, 8,9).

The Maximum Likelihood statistic $detml = -ln(P) = 10.8$ for P=2×10^{-5}, and this threshold $detml$ was applied in EMLDETECT. The numbers of source detections at or above $detml$=10.8 are listed in the left column of Table 5. Cross-matching the sources with $detml$>10.8 in the three bands gives a total of 1761 sources. There are numerous sources with $detml$>10.8 in fewer than three bands. In these cases we can search for significant flux in the other bands to a 100 times higher P, as the area being searched is now 100 times smaller than the whole survey area (for a $5''$ cross-match radius). This corresponds to a threshold $detml = 6$. In the right hand column of Table 5 we give the numbers of sources detected in each band having 6< $detml$ <10.8. Table 6 reports the numbers of catalog sources at or above $detml = 10.8$ in 3 bands, 2 bands, or in only one band. (In this last case the sources must have $detml$>10.8 in order to have been selected at all.)

Almost a thousand (946) XMM-COSMOS sources have also been observed by *Chandra* with an exposure larger than 30 ksec (Cappelluti et al. 2009), and 876 are present in the C-COSMOS catalog. Only 70 sources are not present in the *Chandra* catalog, while 24 XMM-COSMOS sources have been resolved into two separate sources (Brusa et al. 2009; Paper III) due to the better *Chandra* PSF. Of the 70 sources not recovered by *Chandra*, more than half are in regions with low exposure (between 30 and 50 ksec) as, for example, in small gaps of low exposure (Fig.4). The remainder are either sources with only hard XMM detections or, after a visual inspection, they are found to be spurious XMM sources, in agreement with the expected fraction of spurious sources. C-COSMOS and XMM-COSMOS combine to give a total of $\sim$2800 unique COSMOS X-ray sources. The distribution of X-ray

Table 5: Number of sources detected in each band at the two adopted thresholds.

Band	$detml \geq 10.8$	$6 < detml < 10.8$
Full (F)	1655	71
Soft (S)	1340	88
Hard (H)	1017	165

Table 6: Number of sources with $detml \geq 10.8$ in at least one band.

Bands	Number of sources
F+S+H	922
F+S	474
F+H	257
F	73
S	32
H	3
Total	1761

fluxes for the C-COSMOS sources in the Soft and Hard bands is shown in Figure 8. For comparison, we also show the flux distribution of CDFN (dotted line), CDFS (dot-dashed line) and XMM-COSMOS detected sources (dashed line). The *Chandra* and *XMM-Newton* surveys are complementary in that, together, they span almost 3 orders of magnitude in X-ray flux, and have over 100 soft band (and over 50 hard band) sources per 0.16 dex bin over about 1.5 orders of magnitude in flux. The well-defined cut-off in source numbers at faint fluxes, which reflects the tight exposure time distribution (Fig.7), is significantly different from the relatively flat distribution of CDFN (dotted line) and CDFS (dot-dashed line) source fluxes (Fig.8).

The complete catalog contains source positions and source count rates, exposure times, signal-to-noise ratio (S/N), and fluxes in the three bands and hardness ratios (see next section). The catalog is ordered with the sources detected in the Full band first, followed by those detected in the Soft band only and by those detected in the Hard band only.

The resulting catalog is available in the ApJ on-line version and on the 'Chandra COS-MOS Survey' website[18]. Supporting data products (including images, event files and

---

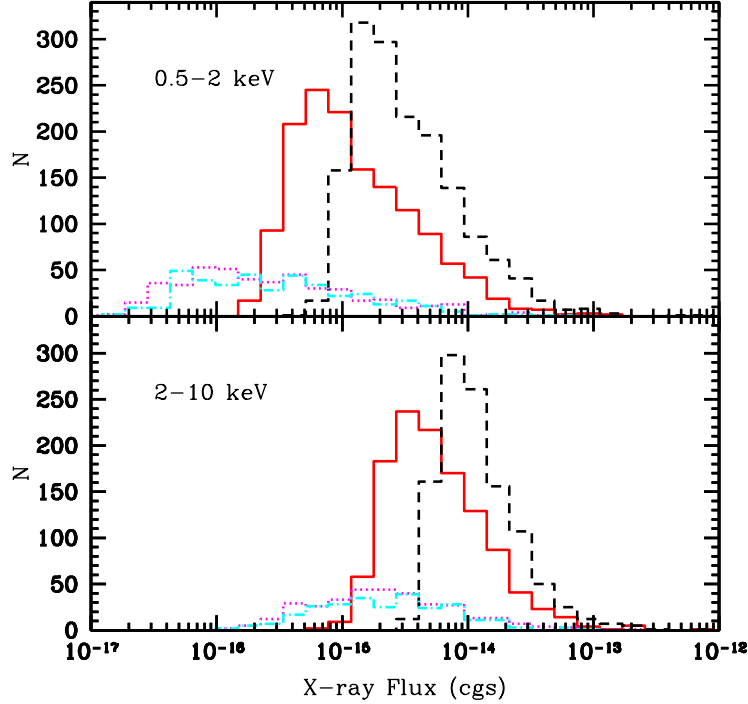[18]http://chandracosmos.cfa.harvard.edu/reports/analysis/20090310_TA_source_catalog_2.1/

Fig. 8.— The distribution of fluxes for sources detected in the Soft and Hard band (continuous line) compared with the flux distribution of CDFN sources (dotted line), CDFS (dot-dashed line) and XMM-COSMOS sources (dashed line). Sources with upper limit have not been included in this figure.

exposure maps) will be available at the '*Chandra* COSMOS Survey' website and at IRSA[19]. At the *Chandra* COSMOS Survey it will also be possible to browse a database that includes 'postage stamps' of the X-ray data for each source, along with the multiwavelength optical and infrared data, including the I-band, K-band and Spitzer 3.6μm (Band 1) images used in Paper III to identify the sources.

5.2.   Catalog Description

The EMLDETECT procedure was run on the three bands: Soft, Hard and Full. In order to be consistent with other results in literature, count rates estimated in the 2–7 keV and 0.5–7 keV energy bands were extrapolated into 2–10 keV and 0.5–10 keV fluxes, respectively,

---

[19]URL: http://irsa.ipac.caltech.edu/data/COSMOS/

using a spectral slope, Γ=1.4. We also report the number counts obtained from aperture photometry (see Paper II).

Table 7 gives the columns of the catalog of the 1761 X-ray sources. A more detailed description of each column is reported below:

- *Column 1*: Chandra source name, following the standard IAU convention with the prefix "CXOC" for 'Chandra X-ray Observatory COSMOS' survey.

- *Column 2*: Source number. Sources are listed in order of detection: first those detected in the Full band with $detml \geq$10.8, followed by those detected in the soft band only and by those detected in the Hard band only.

- *Column 3-4*: Right Ascension and Declination in the J2000 coordinate system.

- *Column 5*: Positional error ($\sqrt{\sigma_{RA}^2 + \sigma_{Dec}^2}$) computed using the following equation $Pos_{error} = PSF_{radius}/\sqrt{S}$ where S is the number of net source counts, after the subtraction of the background, in a circular region of radius corresponding to the 50% encircled energy in the field where the source is at the lowest off-axis angle (Paper II).

- *Column 6-7*: Count rate and count rate error in the Full band (0.5-7 keV). These are *effective* count rates that would apply if the source had been observed at the aim point in every pointing. I.e. computed by dividing the best fit counts for each source by the effective exposure time at the position of each source (the effective exposure time includes corrections for vignetting, dither, bad pixels and spatially-dependent quantum efficiency). The count rate error at 68% confidence level was computed using the equation $error == \frac{\sqrt{C_{s,90\%}+(1+a)B_{90\%}}}{0.9 \cdot T}$, where where C_s are the source counts estimated by *EMLdetect*, corrected to an area including 90% of the PSF[20], B are the background counts evaluated from the background rate (counts/pixel) estimated by *EMLdetect* multiplied for an area of radius R_w, which is the mean of the radii, correspondig to 90% enclosed counts fraction (ECF) of each observation, weighted by the observation exposure relative to the total exposure, and T is the vignetting corrected exposure time at the position of the source from the exposure maps. We use a=0.5, to allow for uncertainties in the background, which is computed through the EMLDETECT procedure (see Paper II for more details).

- *Column 8–9*: Full band 0.5–10 keV fluxes and errors were computed converting count rates to fluxes using the following formula: $Flux = B_{rate}/(CF * 10^{11})$, where B_{rate} is

---

[20]http://cxc.harvard.edu/caldb/

the count rate in each band as described in column 6, CF is the energy conversion factor 0.742 $cts\ erg^{-1}\ cm^2$ (and 1.837 and 0.381 for the Soft and Hard, 2–10 keV band respectively) appropriate for a power law spectrum with spectral index Γ=1.4 and Galactic column density $N_H = 2.7 \times 10^{20} cm^{-2}$. For sources not detected in this band, a 90% upper limit is reported (see Paper II for details).

- *Column 10*: Full band signal to noise ratio.

- *Column 11*: Full band exposure time derived from the exposure map.

- *Column 12–13*: The aperture photometry counts and error in the Full band (0.5–7 keV) are derived from event data for each individual Obsid and CCD where a source lands. Note that ($F\_rate \times f\_exptime$) $\neq$ f_cts_ap. Circular extraction regions corresponding to the 90% ECF for that observation are centered on the source RA, Dec. The individual photometry values are then merged to produce a single set of values accounting for the ECF for each ObsID, given the different extraction regions needed.

- *Column 14*: Exposure time (ksec) from the same region used to generate the aperture photometry.

- *Column 15-23*: Same as columns 6–14 for the Soft band (0.5-2 keV).

- *Column 24-32*: Same as columns 6–14 for the Hard band (2-7 keV). Fluxes and errors are computed for the 2-10 keV band with the conversion factor quoted above.

- *Column 33-35*: Hardness ratio and 90% upper and lower errors computed as follows: H-S/H+S where H are the counts in the Hard band and S the counts in the Soft band. The hardness ratio was calculated starting with the EMLDETECT rate values. Upper and lower limits were calculated using the Bayesian Estimation of Hardness Ratio code (BEHR, Park et al. 2006). Pseudo-source and background count values were generated using the net count rate, background rate (per pixel), and a 3 arcsec source aperture and 5-20 arcsec aperture for background areas. The aperture photometry was unsuitable for this purpose because the individual extraction apertures do not have the constant background/source area ratios required by the assumptions used in BEHR.

5.3. Catalog Completeness & Number Counts

In order to provide an end-to-end check that the many calibration steps taken in deriving the *Chandra* COSMOS point source catalog have been performed correctly, we constructed

Table 7: Data fields in the Catalog.

|		
1	NAME	Chandra source name
2	Source #	source number.
3	RA	Chandra Right Ascension (J2000, hms)
4	DEC	Chandra Declination (J2000, dms)
5	pos_err	Positional error [arcsec]
6	f_rate	0.5–7 keV count rate [counts/sec]
7	f_rate_err	0.5–7 keV count rate error [counts/sec]
8	f_flux	0.5–10 keV Flux [erg cm^{-2}s^{-1}]
9	f_flux_err	0.5–10 keV Flux error [erg cm^{-2}s^{-1}]
10	f_snr	0.5–7 keV S/N Ratio
11	f_exptime	0.5–7 keV exposure time [ksec]
12	f_cts_ap	0.5–7 keV aperture photometry net counts [counts]
13	f_cts_ap_err	0.5–7 keV aperture photometry net counts error [counts]
14	f_exptime_ap	0.5–7 keV exposure time from aperture photometry [ksec]
15	s_rate	0.5–2 keV count rate [counts/sec]
16	s_rate_err	0.5–2 keV count rate error [counts/sec]
17	s_flux	0.5–2 keV Flux [erg cm^{-2}s^{-1}]
18	s_flux_err	0.5–2 keV Flux error [erg cm^{-2}s^{-1}]
19	s_snr	0.5–2 keV S/N Ratio
20	s_exptime	0.5–2 keV exposure time [ksec]
21	s_cts_ap	0.5–2 keV aperture photometry net counts [counts]
22	s_cts_ap_err	0.5–2 keV aperture photometry net counts error [counts]
23	s_exptime_ap	0.5–2 keV exposure time from aperture photometry [ksec]
24	h_rate	2–7 keV count rate [counts/sec]
25	h_rate_err	2–7 keV count rate error [counts/sec]
26	h_flux	2–10 keV Flux [erg cm^{-2}s^{-1}]
27	h_flux_err	2–10 keV Flux error [erg cm^{-2}s^{-1}]
28	h_snr	2–7 keV S/N Ratio
29	h_exptime	2–7 keV exposure time [ksec]
30	h_cts_ap	2–7 keV aperture photometry net counts [counts]
31	h_cts_ap_err	2–7 keV aperture photometry net counts error [counts]
32	h_exptime_ap	2–7 keV exposure time from aperture photometry [ksec]
33	hr	hardness ratio
34	hr_lim_lo	hardness ratio 90% lower limit
35	hr_lim_hi	hardness ratio 90% upper limit
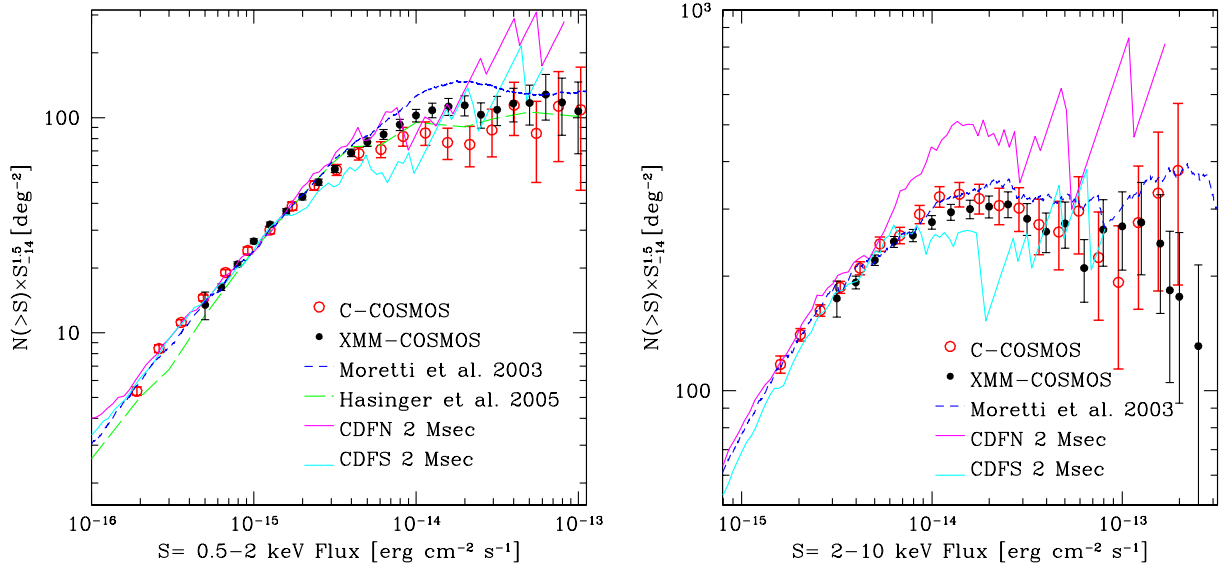
Fig. 9.— The Euclidean-normalized, logN-logS curves for C-COSMOS sources with *detml*>10.8: *left:* Soft band (0.5–2 keV, red open circles), *right:* Hard band (2–10 keV). The XMM-COSMOS curve (black filled circles, Cappelluti et al. 2009), the soft band curve of Hasinger et al. (2005; green line), the Moretti et al. (2003) compilation (blue dashed line), and the CDF-N (magenta solid line, Alexander et al. 2003) and CDF-S (cyan solid line, Luo et al. 2008) curves. The agreement is good over the flux interval where the various surveys have good statistics (see text).

the observed logN-logS curve, i.e. the number of sources, N(>S), detected per square degree brighter than a a given flux, S (erg cm^{-2}s^{-1}) in the Soft (0.5-2 keV) and Hard (2–10 keV) bands. Because at the limiting fluxes the sky coverage is small (Fig.3), and so has a large fractional error, we used the flux limits given in Tab.1, column 3, thus omitting the faintest $\sim$10 sources. X-ray source counts in this flux and energy range have been well studied, giving us a good baseline against which to compare C-COSMOS (Cappelluti et al. 2009).

The results, for sources detected at *detml*>10.8 (Tab. 5, left column) are shown in figure 9, normalized by a Euclidean 1.5 slope to enable differences between various X-ray logN-logS curves to be seen easily. Figure 9 also shows comparisons with several other logN-logS curves: from Moretti et al (2003, blue dashed line), which combines data from ROSAT (for bright sources), XMM-Newton (for intermediate flux sources), and *Chandra* for faint sources; from Hasinger et al. (2005) logN-logS (green dashed line); and from the CDF-N (magenta solid line, Alexander et al. 2003) and CDF-S (cyan solid line, Luo et al. 2008) curves. In the range where these curves overlap and C-COSMOS has good statistics the agreement is excellent, and C-COSMOS extends a factor $\sim$4 below the XMM-COSMOS limit, as expected.

In the Soft band, around $\sim$2×10^{-14} erg cm^{-2}s^{-1}, the C-COSMOS logN-logS shows a $\sim$20-30% underdensity at a 2σ level with respect to the XMM-COSMOS source counts. In order to evaluate this deviation, we estimated the amplitude of the fluctuations expected due to sample and cosmic variance. According to Yang et al. (2004, 2006) and Cappelluti et al. (2009), the fluctuations of the counts in a box of area Ω deg^2 of a population of $\mathcal{N}$ deg^{-2} sources at a given flux limit, is given by a linear combination of a Poisson fluctuations and a cosmic variance component introduced by source clustering:

$$\sigma_{cv}^2 = \mathcal{N} + \frac{\mathcal{N}}{\Omega^2} \int w(\theta)d\theta_1 d\theta_2 \qquad (1)$$

In eq. 1 $w(\theta)$ is the angular autocorrelation function expressed as a $w(\theta) = \frac{\theta}{\theta_0}^{-\gamma}$. According to Cappelluti et al. 2007 eq. 1 can be solved analytically by knowing the slope and the amplitude of $w(\theta)$. By using the source surface density of Soft X-ray sources at 2×10^{-14} erg cm^{-2}s^{-1} (i.e. $\sim$30 source deg^{-2}) on a box of 0.9 deg^2, and assuming the angular autocorrelation function of Miyaji et al. (2007) for XMM-COSMOS (i.e. θ_0=2″, γ=1.8), we determined σ^2 $\sim$36 which corresponds to a fraction variance of 20% of the source counts. We can therefore conclude that a deviation of the size observed can be introduced by a single structure, in an area of XMM-COSMOS not covered by *Chandra*, that generates a fluctuation in the bright source counts at 1.5σ level.

Another check of the source detection efficiency at the brighter C-COSMOS flux levels is a comparison with the XMM COSMOS survey (Hasinger et al. 2007). As shown by

Cappelluti et al. (2009) and Brusa et al. (2009, in preparation), C-COSMOS recovers ∼93% of the XMM sources in the C-COSMOS field, resolving ∼3% into close pairs.

6. Conclusions & Future Work

We have presented the ∼0.9 sq.deg *Chandra* COSMOS survey (C-COSMOS) and a catalog of point sources from that survey. Employing a heavily overlapping tiling of ACIS-I observations has proven an effective method of covering a large area to a well-defined exposure (±12%) and uniform flux limit. The central ∼0.5 sq.deg achieved an exposure of 160 ksec, and the outer ∼0.4 sq.deg achieved an exposure of ∼80 ksec. The equatorial location of COSMOS helped to produce a uniform tiling pattern by allowing an almost constant roll angle for *Chandra* observations over most of the target visibility window. The point source catalog from the C-COSMOS survey has a flux limit of 2×10^{-16} erg cm^{-2}s^{-1} (0.5-2 keV) and contains 1761 sources detected in at least one band with a probability of being spurious of $<2 \times 10^{-5}$ (*detml* ≥ 10.8).

The novel three-stage source detection method employed (Paper II) coped well with the peculiarities of the C-COSMOS tiling scheme and, more generally, is good at separating close pairs of sources, while retaining photometric accuracy. The C-COSMOS sky coverage has a sharp cut-off which produces a homogeneous flux threshold over the whole area and the soft band $logN - logS$ curve for C-COSMOS matches well the Hasinger et al. (2005) determination over a broad flux range, giving us high confidence in the completeness of the catalog down to the limiting flux.

The catalog is available in the ApJ on-line version and on the 'Chandra COSMOS Survey' website (see footnote 16) Supporting data products (including images, event files and exposure maps) are available at the 'Chandra COSMOS Survey' website and at IRSA (see footnote 17).

The sub-arcsecond accuracy of the *Chandra* positions, together with the rich pre-existing deep multiwavelength coverage of the COSMOS field, allows us to reach a 96% identification rate for the C-COSMOS sources with counterparts in both optical and infrared, and 99.7% in at least one band (Paper III).

A parallel effort on the detection of extended sources in the C-COSMOS field finds ∼50 groups and clusters (Finoguenov et al. 2009, in preparation).

We anticipate a rich haul of science results from C-COSMOS. The *Chandra* sources have already resolved ambiguous source identifications from the XMM-COSMOS survey (Hasinger

et al. 2007, Brusa et al. 2007, 2008, Cappelluti et al. 2007, 2009). The paper by Fiore et al. (2008) on the stacking analysis of sources with extreme mid-infrared to optical ratio, presumably Compton Thick AGN, has been recently accepted. Several further papers are in preparation or submitted on: off-nuclear sources in galaxies (Mainieri et al. 2009), X-ray source correlation functions (Miyaji et al. 2009), the 3D cluster/AGN cross-correlation function (Cappelluti et al. 2009), high X-ray/optical flux ratio objects (Civano et al. 2009), high-redshift QSO (Civano et al. 2009), and other topics.

A basic X-ray spectral analysis of the nearly 500 sources with more than 80 counts ($\sim 23\%$ of the total sample) becomes possible. The resulting spectral slopes and absorbing column densities will allow the statistical properties of a large sample at substantial redshift and over a uniform and contiguous field to be studied effectively (Lanzuizi et al. 2009 in preparation).

There is information in C-COSMOS below the current catalog flux limit, thanks to the low background of *Chandra* ACIS. A 'stacking' analysis (Brusa et al. 2002, Hornschemeier et al. 2002, 2003) allows the mean X-ray properties of groups of objects to be determined. Miyaji et al. (2008) have solved the issues created by the C-COSMOS tiling scheme for stacking and papers using this tool are in preparation on z$\sim$1 elliptical galaxies (Kim et al. 2008). The potential uses of stacking in the C-COSMOS field are extensive, thanks to the multiple data sets available from which to choose samples for stacking. For example, there will be $\sim 2 \times 10^4$ galaxies with good optical spectra from z-COSMOS (Lilly et al. 2007) in the C-COSMOS field. This entire sample is well characterized both morphologically via HST imaging, and in terms of stellar population, from the UV to far-IR coverage of the other telescopes that have observed COSMOS (Scoville et al. 2007b). This rich data set will enable galaxy X-ray evolution studies by environment, morphology and luminosity using fine-grained stacks of C-COSMOS data with $\sim$100 galaxies per bin, for an effective exposure time of $\sim$20 Ms per bin.

Clearly the C-COSMOS survey will be of value for some time.

7. Acknowledgements

REFERENCES

Alexander, D. M., et al. 2003, AJ, 126, 539

Arnaboldi, M., Neeser, M. J., Parker, L. C., Rosati, P., Lombardi, M., Dietrich, J. P., & Hummel, W. 2007, The Messenger, 127, 28

Baldi, A., Molendi, S., Comastri, A., Fiore, F., Matt, G., & Vignali, C. 2002, ApJ, 564, 190

Bertoldi, F., et al. 2007, ApJS, 172, 132

Brandt, W. N., Hornschemeier, A. E., Schneider, D. P., Alexander, D. M., Bauer, F. E., Garmire, G. P., & Vignali, C. 2001, ApJ, 558, L5

Brandt, W. N., & Hasinger, G. 2005, ARA&A, 43, 827

Brunner, H., Cappelluti, N., Hasinger, G., Barcons, X., Fabian, A. C., Mainieri, V., & Szokoly, G. 2008, A&A, 479, 283

Brusa, M., et al.. 2002, ApJ, 581, 89

Brusa, M., et al. 2007, ApJS, 172, 353

Capak, P., et al. 2007, ApJS, 172, 99

Cappelluti, N., et al. 2007, ApJS, 172, 341

Cappelluti, N., et al. 2009, ApJaccepetted, arXiv:0901.2347

Civano F., et al. 2009, in preparation, [Paper III]

Damiani, F., Maggio, A., Micela, G., & Sciortino, S. 1997, ApJ, 483, 350

Dickey, J. M., Lockman, F. J., 1990, Ann.Rev.Ast.& Ap., 28, 215

Eckart, M. E., Stern, D., Helfand, D. J., Harrison, F. A., Mao, P. H., & Yost, S. A. 2006, ApJS, 165, 19

Fabbiano G., 2006, ARA&A, 44, 323

Fiore, F., et al. 2003, A&A, 409, 79

Fiore, F., et al. 2008, ApJ, 672, 94

Fruscione, A., et al. 2006, Proc. SPIE, 6270,

Garmire, G. P., Bautz, M. W., Ford, P. G., Nousek, J. A., & Ricker, G. R., Jr. 2003, Proc. SPIE, 4851, 28

Gebhardt, K., et al. 2000, ApJ, 539, L13

Giacconi, R., et al. 2002, ApJS, 139, 369

Gilli, R., Comastri, A., & Hasinger, G. 2007, A&A, 463, 79

Harrison, F. A., Eckart, M. E., Mao, P. H., Helfand, D. J., & Stern, D. 2003, ApJ, 596, 944

Hasinger, G., Miyaji, T., & Schmidt, M. 2005, A&A, 441, 417

Hasinger, G., et al. 2007, ApJS, 172, 29

Hornschemeier, A. E., et al. 2003, AJ, 126, 575

Hornschemeier, A. E., Brandt, W. N., Alexander, D. M., Bauer, F. E., Garmire, G. P., Schneider, D. P., Bautz, M. W., & Chartas, G. 2002, ApJ, 568, 82

Ilbert, O., et al. 2008, ApJ, 690, 1236

Kim, M., et al. 2007, ApJS, 169, 401

Laird, E. S., et al. 2008, ApJS, 180, 102

Lehmer, B. D., et al. 2005, ApJS, 161, 21

Lehmer, B. D., et al. 2006, AJ, 131, 2394

Lilly, S. J., et al. 2007, ApJS, 172, 70

Luo, B., et al. 2008, ApJS, 179, 19

Magorrian, J., et al. 1998, AJ, 115, 2285

Manners, J. C., et al. 2003, MNRAS, 343, 293

Marconi, A., & Hunt, L. K. 2003, ApJ, 589, L21

Merritt, D., & Ferrarese, L. 2001, MNRAS, 320, L30

Miyaji, T., et al. 2007, ApJS, 172, 396

Mobasher, B., et al. 2007, ApJS, 172, 117

Moretti, A., Campana, S., Lazzati, D., & Tagliaferri, G. 2003, ApJ, 588, 696

Murray, S. S., et al. 2005, ApJS, 161, 1

Nandra, K., Mushotzky, R. F., Arnaud, K., Steidel, C. C., Adelberger, K. L., Gardner, J. P.,
    Teplitz, H. I., & Windhorst, R. A. 2002, ApJ, 576, 625

Nandra, K., et al. 2005, MNRAS, 356, 568

Park et al. 2006, ApJ, 652, 610

Puccetti, S., et al. 2006, A&A, 457, 501

Puccetti S., et al. 2009, in preparation, [Paper II]

Salvato, M., et al. 2009, ApJ, 690, 1250

Sanders, D. B., et al. 2007, ApJS, 172, 86

Schinnerer, E., et al. 2007, ApJS, 172, 46

Scott K.S., et al. MNRAS, 385, 2225

Scoville, N., et al. 2007a, ApJS, 172, 1

Scoville, N., et al. 2007b, ApJS, 172, 38

Scoville, N., et al. 2007c, ApJS, 172, 150

Taniguchi, Y., et al. 2007, ApJS, 172, 9

Tremaine, S., et al. 2002, ApJ, 574, 740

Trump, J. R., et al. 2007, ApJS, 172, 383

van Speybroeck L.P. et al. 1997, SPIE, 3113, 89

Weisskopf, M. C., Brinkman, B., Canizares, C., Garmire, G., Murray, S., & Van Speybroeck, L. P. 2002, PASP, 114, 1

Wright, E.L., 2006, PASP, 118, 171

Yang, Y., Mushotzky, R. F., Steffen, A. T., Barger, A. J., & Cowie, L. L. 2004, AJ, 128, 1501

Yang, Y., Mushotzky, R. F., Barger, A. J., & Cowie, L. L. 2006, ApJ, 645, 68

Zamojski, M. A., et al. 2007, ApJS, 172, 468

Figure caption:

Plot of $N(>S) \times S_{-14}^{1.5}$ [deg^{-2}] versus $S = 2$-10 keV Flux [erg cm^{-2} s^{-1}].

Legend:
- ○ C-COSMOS
- ● XMM-COSMOS
- - - - Moretti et al. 2003
- —— CDFN 2 Msec
- —— CDFS 2 Msec
- ▲ Mateos et al. 2008